LETTER

Quantum anomalous Hall effect of Dirac half-metal monolayer $TiCl_3$ with high Chern number

To cite this article: Ze Liu *et al* 2021 *EPL* **136** 27004

A Letters Journal Exploring the Frontiers of Physics

October 2021

EPL, **136** (2021) 27004
doi: 10.1209/0295-5075/ac23e9

www.epljournal.org

Quantum anomalous Hall effect of Dirac half-metal monolayer $TiCl_3$ with high Chern number

Ze Liu[1], Guang Yang[2,3], Xiujuan Mao[1], Linyang Li[4] and Jia Li[1,4(a)]

[1]*School of Materials Science and Engineering, Hebei University of Technology - Tianjin 300401, China*
[2]*Beijing National Laboratory for Condensed Matter Physics, Institute of Physics, Chinese Academy of Sciences Beijing 100190, China*
[3]*School of Physics Sciences, University of Chinese Academy of Sciences - Beijing 100049, China*
[4]*School of Science, Hebei University of Technology - Tianjin 300401, China*

received 23 June 2021; accepted in final form 6 September 2021
published online 7 February 2022

Abstract – Based on first-principles calculations, monolayer $TiCl_3$ is predicted to be a 100% spin-polarized Dirac half-metal with ferromagnetic Curie temperature T_c of 63 K as predicted from Monte Carlo simulations. When considering the spin-orbit coupling, the Dirac point in the spin-up opens a ∼3 meV band gap. The calculated result of the anomalous Hall conductivity shows the Chern number $C = 3$, indicating that three corresponding gapless chiral edge states have emerged inside the bulk gap. Our findings suggest a feasible new member of the quantum anomalous Hall insulator family with promising applications in spintronic devices without dissipation edge states.

Introduction. – The quantum Hall effect (QHE) is one of the most important and basic quantum effects in condensed matter physics. This phenomenon was discovered in 1980 by von Klitzing *et al.* when they studied the two-dimensional (2D) electron gas in Si/SiO_2 under extremely low temperatures and strong magnetic fields [1,2]. The QHE has attracted great attention due to its potential applications in low-energy consumption and high-speed electronic devices because of the absence of dissipation edge states. However, the application of QHE in electronic devices is primarily limited by the strong magnetic field needed to generate the Landau levels [3]. The quantum anomalous Hall effect (QAHE) [4,5] is a special kind of QHE that can be realized without the need of an external magnetic field. The internal magnetic exchange interaction (ferromagnetic (FM) or antiferromagnetic (AFM) order) can break the time reversal symmetry (TRS) and open a nontrivial gap by spin orbital coupling (SOC) [6,7]. This phenomenon results in a quantized anomalous Hall conductivity (AHC), which is determined by the topological character [8,9] of the band structure and characterized by the Chern number [10,11]. These characteristics lead to the broad application of the quantum anomalous Hall insulators, which are also called Chern insulators, in spintronic devices. QAHE can be directly achieved by introducing the FM order into the topological insulator (also called as the quantum spin Hall insulator) [12,13] to break its TRS and convert its spiral edge states into chiral states. However, the FM Chern insulator [14,15] is difficult to find because of the scarcity of FM insulators in nature. Since the Haldane model [16] was proposed in 1988, abundant theoretical studies on the QAHE [17–19], have been performed, but little experimental progress has been achieved for more than a decade. A promising way is to introduce magnetic impurities to break the TRS in the topological insulator [20]. QAHE was first discovered experimentally through the theoretically proposed chromium-doped magnetic topological insulator $(Bi, Se)_2Te_3$ [21], and the quantized Hall conductance was observed at ultralow temperature (below 30 mK) by Xue *et al.* in 2013 [22]. However, the main challenge in observing QAHE is the very low temperature needed to reach the quantitative platform. Hence, materials possessing QAHE with high Curie temperature (T_c), large band gap, and high carrier mobility [23] are desirable to be explored.

Transition metal (TM) halides TMX_3 [24,25] (X = Cl, Br, I) have paved the way for magnetic ordering in 2D systems [26–28]. In addition to potential applications in spintronics, these materials have received widespread attention in other fields. Given the weak interlayer van der Waals interactions [29,30], the three-dimensional (3D) layered TMX_3 materials [31,32] can be easily exfoliated down

(a)E-mail: jiali@hebut.edu.cn (corresponding author)

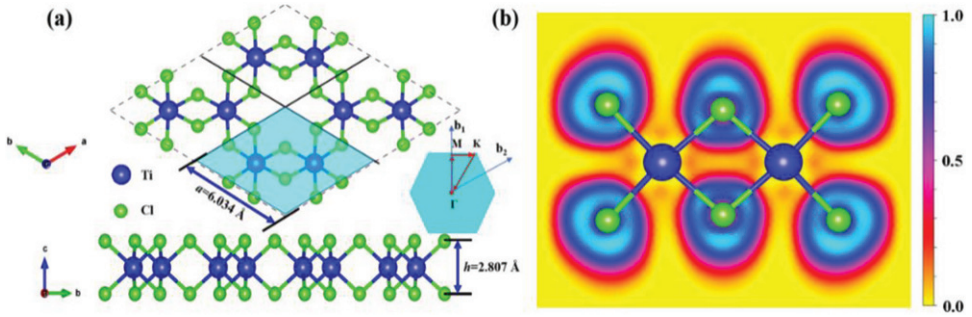

Fig. 1: (a) Top and side views of the 2D $TiCl_3$ crystal structure with the super cell, where the blue and light green spheres denote the Ti and Cl atoms, respectively. The colored areas denote the unit cell of the $TiCl_3$ lattice and the hexagonal BZ, where the reciprocal lattice vectors b_1 and b_2 are indicated. (b) ELF of the monolayer $TiCl_3$, where ELF = 1 (blue) and 0 (yellow) indicate the accumulation and depletion of electron density, respectively.

to 2D monolayers, where the TM atoms are uniformly distributed in a honeycomb structure. Monolayer of TMX_3 with a large band gap and high T_c has recently been proposed to achieve the QAHE. For example, it has been reported that the relatively weak interlayer van der Waals interactions of 3D CrI_3 [33] and $RuCl_3$ were exfoliated from the bulk phase [34] into a 2D material, and the result of first-principles calculations indicates that $RuCl_3$ can realize QAHE [25]. In particular, a pseudospin-1/2 Mott phase on a honeycomb lattice α-$RuCl_3$ can host the celebrated 2D Kitaev model, which has an elusive quantum spin liquid ground state [35]. These findings prompted us to further investigate 2D TMX_3 with novel properties.

In this study, based on the first-principles calculations, monolayer $TiCl_3$ is found to host the topologically nontrivial state and is classified as a Dirac half-metal (DHM) [36,37]. The DHM is characterized by a band gap in one channel and a Dirac cone in the other channel. Moreover, when the SOC is considered, an opened gap of ∼3 meV is found, leading to the QAH states. In addition, the results of calculated magnetic properties of monolayer $TiCl_3$ indicate that its magnetic ground state is FM order with the estimated T_c of 63 K. We further confirm that the 2D $TiCl_3$ has a nontrivial topological Dirac gap state, which is characterized by the Chern number $C = 3$ and chiral edge states. The combination of these properties makes the 2D $TiCl_3$ a promising platform for future applications in electronics and spintronics.

Computational methods. – First-principles calculations were performed by using the spin-polarized density functional theory (DFT) [38] implemented in the Vienna *Ab-initio* Simulation Package (VASP) [39]. The generalized gradient approximation (GGA) [40], as formulated by Perdew, Burke, and Ernzerhof (PBE) [41], was used to treat the exchange and correlation functions. The electron core interactions were characterized by the projector augmented wave (PAW) method [42]. The plane wave cutoff energy was set to 500 eV in all computations. To avoid the image interaction from the periodic boundary conditions, a large vacuum area of 20 Å was applied to the vertical direction of monolayer $TiCl_3$. In all calculations, the energy convergent criterion was 10^{-5} eV per unit cell, and the forces on all relaxed atoms were less than 0.01 eV $Å^{-1}$. Given the size of the system and the accuracy of calculation, the Brillouin Zone (BZ) integration was sampled by using 13×13×1 and 15×15×1 Γ-centered Monkhorst-Pack k grid in calculating the structural relaxation and electronic structures, respectively [43]. To verify the GGA results, we also repeated our calculations by using the GGA+U method [44]. The combination of DFT and Hubbard U correction was also used to investigate the effect of on-site Coulomb repulsion of the Ti $3d$ orbitals. To confirm the dynamic stability, we performed the phonon dispersion calculations by using the force constants method (VASP-DFPT) implemented in the PHONOPY code [45], in which a 2×2×1 supercell was constructed to calculate the atomic forces by using VASP. The energy cutoff was 500 eV for the plane-wave basis, and the energy convergence criterion was 10^{-10} eV. To examine the thermal stability of monolayer $TiCl_3$, a 3×3×1 supercell was employed in *ab initio* molecular dynamics (AIMD) [46] simulations with the canonical (NVT) ensemble at the temperature of 500 K, by using the Nosé-Hoover thermostat with a step of 1 fs. The Berry curvatures and surface state were calculated using an effective tight-binding Hamiltonian with SOC based on the maximally localized Wannier functions via the WANNIER90 [47]. The iterative Green's function method was used with the package WannierTools [48].

Structure and stability of monolayer $TiCl_3$. – The 2D crystal structure of monolayer $TiCl_3$ (space group $P\bar{3}1m$) is similar to the hexagonal lattice of CrI_3 [49] (see fig. 1(a)), where each Ti atom is bonded with six Cl atoms leading to a distorted octahedral conformation. The Ti atomic layer is sandwiched between two Cl atomic layers, resulting in two Ti and six Cl atoms per (1×1) unit cell. The optimized vertical distance h between the two Cl atom planes is 2.807 Å. The optimized lattice constant a (6.034 Å) and chemical bond distance of Ti-Cl

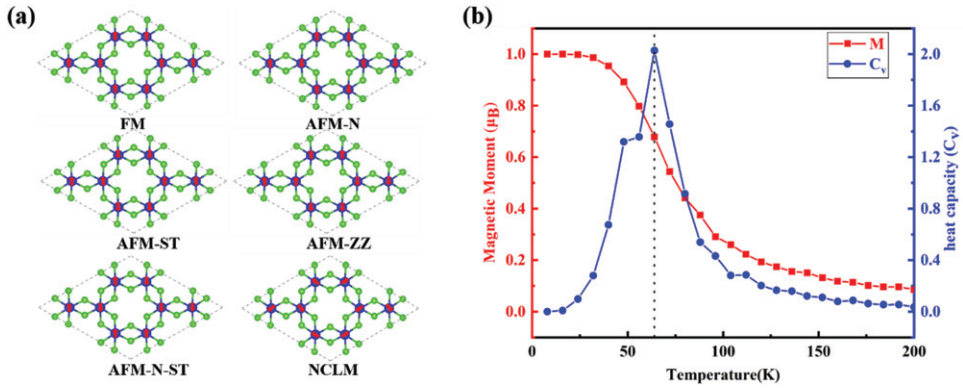

Fig. 2: (a) Top view of the FM, AFM-N, AFM-ZZ, AFM-ST, AFM-N-ST and NCLM spin configurations. The red arrows represent the direction of the magnetic moment. (b) Calculated variations in the average magnetic moment (red) and specific heat (blue) with respect to the temperature for the monolayer $TiCl_3$.

(2.406 Å) are smaller than the lattice constant (7.079 Å) and the chemical bond distance of Cr-I (2.771) of monolayer CrI_3 [31], respectively. The shorter Ti-Cl bond length indicates that the chemical bonding in $TiCl_3$ is stronger than the 2D CrI_3, which will in turn help stabilize the honeycomb structure. This condition is confirmed by the electron localization function (ELF) [50] of monolayer $TiCl_3$ as shown in fig. 1(b). Charge density localization is found in the vicinity of the Cl anion, but no charge density is found between the Ti and Cl atoms. This result reflects the characteristics of the ionic bonds in $TiCl_3$; that is, each Ti atom provides three electrons to its six bonded Cl atoms. To evaluate the structural stability of monolayer $TiCl_3$, we also calculated its formation energy. The result of calculation is $-1.57\,\mathrm{eV/atom}$, which indicates that the monolayer $TiCl_3$ will form a strongly bonded network. To verify the dynamic and thermodynamic stability of monolayer $TiCl_3$, we perform the phonon and AIMD simulations, respectively. The results (see figs. S1(a) and (b) in the Supplementary Material `Supplementarymaterial.pdf` (SM)) signify that the monolayer $TiCl_3$ is dynamically and thermally stable above room temperature.

Magnetic property of monolayer $TiCl_3$. – To determine the ground state magnetic properties of monolayer $TiCl_3$, we conducted spin-polarized calculations of the 2×2×1 unit cell with the FM, various AFM phases and also a non-collinear magnetization phase, such as the Néel-antiferromagnetic (AFM-N), zigzag-antiferromagnetic (AFM-ZZ), stripy-antiferromagnetic (AFM-ST), mixed Néel-stripy-antiferromagnetic (AFM-N-ST) and non-collinear magnetization (NCLM) orders (see fig. 2(a)). The calculated results reveal that monolayer $TiCl_3$ has an FM order under the ground state because of its lowest energy. The average supercell magnetic moment is $\sim 8\,\mu_B$ ($2\,\mu_B$ per unit cell) with 1 μ_B moment per Ti atom. The magnetic moment is consistent with the +3 oxidation state of Ti and hence the $4s^0 3d^1$ electronic configuration. We also calculated the energy difference between the four AFM, NCLM and FM orders, that is, $\Delta E = E_X - E_{FM}$, where E_X indicates the energy of AFM or NCLM. The results show that the AFM-ZZ is the most stable magnetic order among the four AFM orders and NCLM, because it has the lowest ΔE among the four AFM and NCLM orders (ΔE values for AFM-ZZ, AFM-N, AFM-ST, AFM-N-SR and NCLM are 36.1, 931.1, 147.9, 316.9 meV and 403.4 meV, respectively). Magnetic anisotropy energy (MAE) is also one of the important parameters to characterize magnetic materials [51]. It refers to the energy barrier between the magnetizations of the hard axis and the easy axis. To determine the easy axis for the FM state in the monolayer $TiCl_3$, we have adopted the DFT+SOC calculations to estimate MAE because Ti atoms belong to the $3d$ transition metals. The results of calculation indicate that the easy axis is along the z-direction (out-of-plane), and the magnetization along the z-direction is lower than that along the x and y directions by 0.156 meV and 0.153 meV per unit cell, respectively. We used the AFM-ZZ order as the AFM state in calculating the Curie temperature (T_c), and the T_c of monolayer $TiCl_3$ is 140 K and can be overestimated [15,52]. (The calculation method for Curie temperature is described in sect. S2 of the SM). Thus, we employed Monte Carlo (MC) [53] simulations for a 80×80×1 supercell to reduce the translational constraint, using 10^7 loops for each temperature. The temperature-dependent Ti magnetic moment and special heat capacity for monolayer $TiCl_3$ is plotted in fig. 2(b). The magnetic moment decreases rapidly when the temperature is higher than 63 K. To elucidate the FM paramagnetic transition, we calculated the heat capacity (C_V), which can be simply expressed as follows:

$$C_V = \lim_{\Delta T \to 0} \frac{\Delta E_T}{\Delta T}, \tag{1}$$

where ΔE_T is the change in the total energy as the temperature increases from T to $T+\Delta T$. From the graph of the relationship between C_V and temperature in fig. 2(b), the Curie temperature is 63 K, and the FM paramagnetic

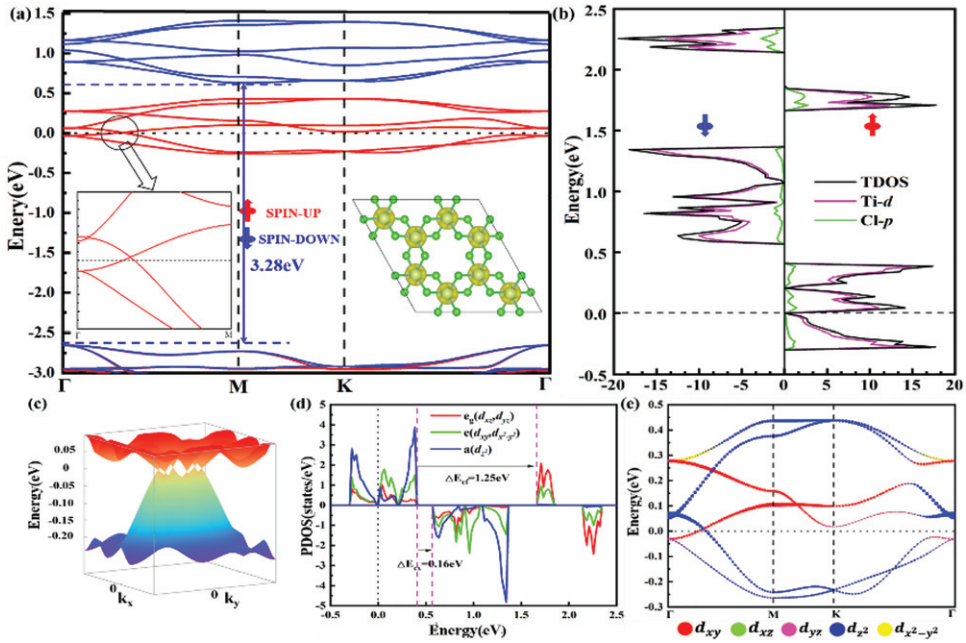

Fig. 3: (a) Spin polarized band structure of the monolayer $TiCl_3$. The red and blue curves correspond to the spin up and spin down channels, respectively. The left inset is a partial enlarged view of the Dirac point between the high symmetry point Γ and M, and the right inset shows the spin density of monolayer $TiCl_3$. (b) Calculated total, Ti-d and Cl-p projected DOS (PDOS) for the monolayer $TiCl_3$. (c) The 3D band structure without SOC around the Fermi level in the 2D k space. (d) The PDOS of d states for Ti atoms at the majority spin channel. (e) Projected band structures of majority spin channel. The relative size of each symbol indicates the Ti atoms projection of the eigenvalue. The Fermi level is denoted by the dashed line.

transition is a second-order phase transition. These results indicate the possibility of stabilizing the FM order of $TiCl_3$ at a finite temperature.

Electronic structure of monolayer $TiCl_3$. – To analyze the electronic properties of the ground-state monolayer $TiCl_3$, we plotted the calculated band structure and density of states (DOS) under the FM state in figs. 3(a) and (b), respectively. The results show that the minority spin channel is insulating with a rather large gap of ∼3.28 eV. The majority spin channel shows a gapless semiconductor feature with a linear dispersion relation around the Fermi level, which is called DHM with 100% spin polarization. As shown by the plotted 3D band profile in fig. 3(c), six spin-polarized Dirac fermions near the Fermi level exist in the majority spin channel in the first BZ. Therefore, the 2D $TiCl_3$ is a full spin-polarized DHM. The spin density distribution of monolayer $TiCl_3$ is shown in the inset of fig. 3(a). The spin is mainly localized around the Ti atoms and little spin is around the Cl atoms. Moreover, the spin-resolved DOS of monolayer $TiCl_3$ is mainly contributed by the 3d orbitals of the Ti atoms (see fig. 3(b)), which is in agreement with the result of the spin density distribution. Therefore, to better understand the electronic property of the Dirac point, we illustrated the projected density of states (PDOS) and the projected band structures of the Ti-3d orbitals for the majority spin channel in figs. 3(d) and (e), respectively. Under the distorted Cl octahedral crystal field, the Ti-3d orbitals are split into triplet t_{2g} ($d_{xy}, d_{x^2-y^2}, d_{z^2}$) and double e_g (d_{xz}, d_{yz}) states. The structural distortion of the $TiCl_3$ octahedron further splits the t_{2g} state into the a (d_z^2) and double e ($d_{xy}, d_{x^2-y^2}$) states. The one spin-up d electron causes the partially filled d orbital, resulting in the metal character and exhibiting a low spin $d^{\uparrow 1}$ electronic configuration. According to Griffith's crystal field theory [54], the spin states of the TM ions can be determined by the relative strength between the crystal field splitting ($\Delta E_{\rm cf}$) and Hund exchange splitting ($\Delta E_{\rm ex}$) of d orbitals. The exchange splitting (0.16 eV) is smaller than the crystal field splitting (1.25 eV) for monolayer $TiCl_3$ resulting in a low-spin (1 $\mu_{\rm B}$) state. This result is in good agreement with the Ti ($d^{\uparrow 1}$) spin configuration. The states near the Fermi level have main contributions from the t_{2g} state, while the e_g state does not contribute significantly as shown in fig. 3(e). The linearly dispersive majority spin electronic band at the Fermi energy results from the hybridization of the Ti derived d_z^2 and d_{xy} states.

SOC-induced quantum anomalous Hall effect. – Dirac materials, such as graphene, silicene, germanene, and tinene, are characterized by the Dirac states constituted of p-orbitals with weak SOC [55]. Therefore, the opened gap by SOC is ∼0.02 meV, making these materials the Z_2 topological insulators with TRS-protected chiral edged states. However, the Dirac states of monolayer $TiCl_3$, which are mainly derived from the 3d orbitals of Ti atoms (see fig. 3(b)) lead to a larger gap of ∼3 meV

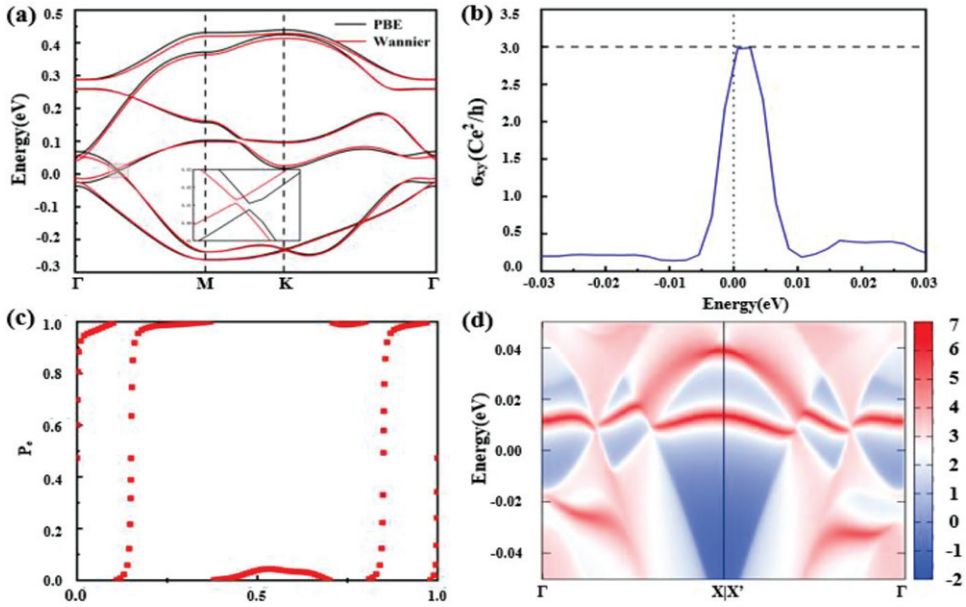

Fig. 4: (a) The band structure of the monolayer $TiCl_3$ with SOC obtained from the PBE (black) and Wannier (red). The illustration is an enlarged view of the Dirac point. (b) The AHC when we shifted the Fermi level around its original Fermi level. (c) The change in the electronic polarization P_e. (d) The calculated chiral edge states for semi-infinite boundary of monolayer $TiCl_3$.

(see fig. 4(a)). The SOC gap of the Ti-d orbitals with the broken TRS may lead to the Chern insulator and QAHE.

To further study the topological properties of monolayer $TiCl_3$, we first calculated its Chern insulator states characterized by the non-zero Chern number (C), which will be finite integer value if QAHE can be realized in the material. The C from the integral of the Berry curvature $\Omega(k)$ in the first BZ can be determined using the Kubo formula [56,57]:

$$\Omega(k) = -2\sum_n f_n \sum_{m\neq n} \times \mathrm{Im}\frac{\langle \Psi_n(k)|\nu_x|\Psi_m(k)\rangle\langle \Psi_m(k)|\nu_y|\Psi_n(k)\rangle h^2}{(E_m(k)-E_n(k))^2}, \quad (2)$$

$$C = \frac{1}{2\pi}\int_{\mathrm{BZ}} \mathrm{d}^2k\Omega(k), \quad (3)$$

where f_n is the Fermi-Dirac distribution function; ν_x and ν_y are the velocity operators along the x and y directions, respectively; $\Psi_n(k)$ is the Bloch wave function; E_n is the eigenvalue; and the summation is the overall n occupied bands below the Fermi level (m represents the unoccupied bands above the Fermi level). The absolute value of the C is equal to the number of gapless edge states along the edge of the $TiCl_3$ sheet. The calculated result shows that the C of the system is 3, indicating the presence of three chiral edge states. The C is not only an integer but also gives rise to the AHC $\sigma_{xy} = Ce^2/h$, showing a quantized charge Hall plateau in terms of e^2/h (e stands for the electronic charge, and h indicates the Planck constant) when the Fermi level is located in the insulating gap of the majority spin Dirac cone. The calculated AHC is shown in fig. 4(b). A nontrivial gap of ∼3 meV and a $C = 3$ can be inferred from the plateau near the Fermi level. Thus, our proposed monolayer $TiCl_3$ is a Chern insulator with a finite C.

The nonzero C can also be determined by evaluating the electronic polarization P_e at discrete points in the primitive reciprocal lattice vector $k_y = k_i$ [58]. In another primitive reciprocal lattice vector k_x, the hybrid Wannier charge centers (HWCCs) [59] can be defined as follows:

$$\overline{x}_n(k_y) = \frac{i}{2\pi}\int_{-\pi}^{\pi} \mathrm{d}k_x \langle u_n(k_x,k_y)|\partial k_x|u_n(k_x,k_y)\rangle, \quad (4)$$

where $u_n(k_x,k_y)$ is the periodic part of the Bloch function $\Psi_n(k)$. The sum $\overline{x}_n$ of the HWCCs gives the hybrid electronic polarization $P_e = e\sum_n \overline{x}_n(k_y)$, in which the HWCCs, $\overline{x}_n(k_y)$, and P_e are the smooth functions of k_y for $k_y \in [0, 2\pi]$. This result leads to a clearly defined physically observable ΔP_e under a continuous deformation of the system. Therefore, the C is given by $C = \frac{1}{e}\Delta P_e = \frac{1}{e}[P_e(2\pi) - P_e(0)]$. Figure 4(c) shows the calculated electronic polarization P_e. P_e shifts upwards with the winding number 3, indicating that the C is equal to 3. This result implies that monolayer $TiCl_3$ is a QAH insulator with a topological nontrivial gap.

The topologically protected chiral edge state is one of the most important consequences of the QAH state. To further reveal the non-trivial topological properties of monolayer $TiCl_3$, we also calculated the edge states by constructing a semi-infinite boundary $TiCl_3$ with the maximally localized Wannier function Hamilton [60]. As

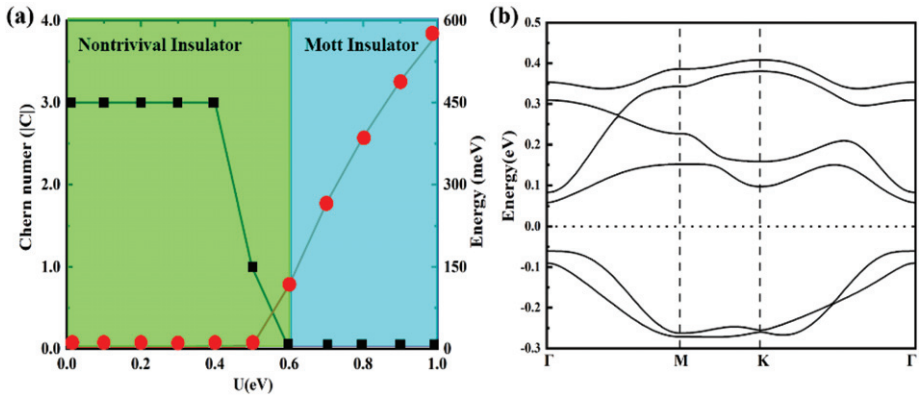

Fig. 5: (a) Calculated band gap (red circle) and Chern number (C) (black square) of the monolayer $TiCl_3$ with Ti spins in the FM configuration as a function of U value for GGA+SOC+U method. (b) Band structure of monolayer $TiCl_3$ with SOC for $U = 0.6$ eV.

shown in fig. 4(d), the nontrivial edge states connecting the valence and conduction bands cross the insulating gap of the Dirac cone. The appearance of the three chiral edge states is consistent with the calculated $C = 3$, confirming the nontrivial topological properties of monolayer $TiCl_3$.

The size of the topological nontrivial bulk gap plays a vital role in the experimental observation of the edge state. The small gap size of monolayer $TiCl_3$ limits its application of QAHE at high temperature and hinders the experimental observation. Moreover, the $3d$ electrons of Ti ions have a great effect on the opening of the band gap near the Fermi level. To obtain a more accurate bulk gap, we performed the DFT combined with Hubbard U correction to investigate the effect of the on-site Coulomb repulsion of the Ti-$3d$ orbitals by varying the effective value of U from 0.0 eV to 1.0 eV. The variation of band gap for monolayer $TiCl_3$ as a function of U is displayed in fig. 5(a). In the presence of SOC, the correlation energy U triggers a large gap in the majority spin channel between the highly symmetrical Γ and K points, and the opened gap increases with increasing U. Variation of the C for monolayer $TiCl_3$ as a function of U is also displayed in fig. 5(a). A nontrivial state with a large C appears at the Fermi level when $U < 0.6$ eV. With further increase in the effective on-site Hubbard-Coulomb interaction, the C decreases and vanishes at the critical $U_c = 0.6$ eV, where the 2D system undergoes a transition from a nontrivial insulator with $C \neq 0$ to the Mott insulator [61] with $C = 0$. This process is accompanied by a very sharp increase in the band gap from a few millielectron-volts to 112 meV. A similar continuous topological quantum phase transition had been reported in $OsCl_3$ [62] and ReI_3 [30]. Figure 5(b) shows the band structure of monolayer $TiCl_3$ with SOC for $U_c = 0.6$ eV. The band gap is ∼0.12 eV, and the Dirac cone disappears completely. This phenomenon may be the reason for the transition from nontrivial insulator to the Mott insulator. To date, monolayer $TiCl_3$ has hardly been investigated among the transition metal halides. Therefore, our present study may lead to further widespread attention for these materials, such as the SOC Mott insulator $RuCl_3$ [63], due to the possibility of realizing Kitaev quantum spin liquid phase [64].

Conclusions. – In summary, we have predicted that 2D monolayer $TiCl_3$ is a DHM material and has many fascinating properties, such as massless Dirac fermions and 100% spin polarization using first-principles calculations. The results of the formation energy, phonon spectrum, and AIMD analysis indicate that the monolayer $TiCl_3$ is dynamically and thermodynamically stable. The Monte Carlo simulations based on the Ising model verify that the Curie temperature of the monolayer $TiCl_3$ can be as high as 63 K. Without including the SOC interaction, a Dirac point in the majority spin channel appears near the Fermi level, and this phenomenon is contributed by the Ti-d orbitals. The mechanism of the Dirac point has been elucidated by considering the magnetic exchange interactions, crystal field, and orbital hybridization. Once the SOC is considered, the symmetry-protected Dirac point opens a band gap of ∼3 meV. We have also demonstrated the possibility of realizing the intrinsic QAHE with high Chern number ($C = 3$), AHC, electronic polarization P_e, and gapless chiral edge states in the monolayer $TiCl_3$, when we considered the SOC in the FM order of magnetic moments. Moreover, when the Hubbard U gradually increases from 0 eV to 0.6 eV, the monolayer $TiCl_3$ undergoes a transition from the topological nontrivial phase to trivial Mott insulator. Therefore, the monolayer $TiCl_3$ can be broadly applied in electronic and spintronic devices.

* * *

We would like to acknowledge the support from the National Natural Science Foundation of China (Grant Nos. 61671199, 12004097) and Natural Science Foundation of Hebei Province (Grant Nos. A2020202010, A2020202031).

Data availability statement: The data that support the findings of this study are available upon reasonable request from the authors.

REFERENCES

[1] Kane C. L. *et al.*, *Phys. Rev. Lett.*, **88** (2002) 036401.
[2] Zhang Y. *et al.*, *Nature (London)*, **438** (2005) 7065.
[3] Haldane F. D. M., *Phys. Rev. Lett.*, **61** (1988) 2505.
[4] He K. *et al.*, *Natl. Sci. Rev.*, **1** (2014) 38.
[5] Liu C. X. *et al.*, *Phys. Rev. Lett.*, **101** (2008) 146802.
[6] Fang C. *et al.*, *Phys. Rev. B*, **92** (2015) 081201.
[7] Lee K. W. and Lee C. E., *Curr. Appl. Phys.*, **20** (2020) 413.
[8] Henk J. *et al.*, *Phys. Rev. Lett.*, **109** (2012) 076801.
[9] Tamai A. *et al.*, *Phys. Rev. X*, **6** (2016) 031021.
[10] Li J. *et al.*, *Nanoscale*, **12** (2020) 3888.
[11] Lian B. *et al.*, *Phys. Rev. Lett.*, **124** (2020) 126402.
[12] Marrazzo A. *et al.*, *Phys. Rev. Lett.* **120** (2018) 117701.
[13] Si N. *et al.*, *J. Phys. Chem. Lett.*, **11** (2020) 1317.
[14] Liu Z. *et al.*, *Phys. Rev. Lett.*, **109** (2012) 186805.
[15] He J. *et al.*, *Nanoscale*, **9** (2017) 2246.
[16] Thonhauser T. and Vanderbilt D., *Phys. Rev. B*, **74** (2006) 235111.
[17] Xu G. *et al.*, *Phys. Rev. Lett.*, **107** (2011) 186806.
[18] Kong X. *et al.*, *Nanoscale*, **10** (2018) 8153.
[19] Tanaka M. *et al.*, *Nano Lett.*, **20** (2020) 7476.
[20] Chen Y. L. *et al.*, *Science*, **325** (2009) 5937.
[21] Zhang H. *et al.*, *Nat. Phys.*, **5** (2009) 438.
[22] Chang C.-Z. *et al.*, *Science*, **340** (2013) 6129.
[23] Weng H. *et al.*, *Adv. Phys.*, **64** (2015) 227.
[24] Huang C. *et al.*, *Phys. Rev. Lett.*, **120** (2018) 147601.
[25] Huang C. *et al.*, *Phys. Rev. B*, **95** (2017) 045113.
[26] Wang H. *et al.*, *Nanoscale*, **6** (2014) 12250.
[27] Sun Q. and Kioussis N., *Phys. Rev. B*, **97** (2018) 094408.
[28] Sun Q. and Kioussis N., *Nanoscale*, **13** (2019) 6101.
[29] Tkatchenko A. and Scheffler M., *Phys. Rev. Lett.*, **102** (2009) 073005.
[30] Liu Y. *et al.*, *Nature (London)*, **567** (2019) 7748.
[31] Liu J. *et al.*, *Phys. Chem. Chem. Phys.*, **18** (2016) 8777.
[32] Valeria Nicolosi *et al.*, *Science*, **340** (2013) 1226419.
[33] Huang B. *et al.*, *Nat. Nanotechnol.*, **13** (2018) 544.
[34] Miró P. *et al.*, *Chem. Soc. Rev.*, **43** (2014) 6537.
[35] Ziatdinov M. *et al.*, *Nat. Commun.*, **7** 2016 13774.
[36] Ishizuka H. and Motome Y., *Phys. Rev. Lett.*, **109** (2012) 237207.
[37] Liu Z. *et al.*, *Nano. Res.*, **10** (2017) 1972.
[38] Car R. and Parrinello M., *Phys. Rev. Lett.*, **55** (1985) 2471.
[39] Kresse G. and Furthmüller J., *Phys. Rev. B*, **54** (1996) 11169.
[40] Perdew J. P. *et al.*, *Phys. Rev. Lett.*, **77** (1996) 3865.
[41] Ernzerhof M. and Scuseria G. E., *J. Chem. Phys.*, **110** (1999) 5029.
[42] Blochl P. E., *Phys. Rev. B*, **50** (1994) 17953.
[43] Monkhorst H. J. and Pack J. D., *Phys. Rev. B*, **13** (1976) 5188.
[44] Dudarev S. L. *et al.*, *Phys. Rev. B*, **57** (1998) 1505.
[45] Parlinski K. *et al.*, *Phys. Rev. Lett.*, **78** (1997) 4063.
[46] Nosé S., *J. Chem. Phys.*, **81** (1984) 511.
[47] Mostofi A. A. *et al.*, *Comput. Phys. Commun.*, **178** (2008) 685.
[48] Wu Q. *et al.*, *Comput. Phys. Commun.*, **224** (2018) 405.
[49] Huang B. *et al.*, *Nature (London)*, **546** (2017) 7657.
[50] Silvi B. and Savin A., *Nature (London)*, **371** (1994) 6499.
[51] Gambardella P. *et al.*, *Science*, **300** (2003) 5622.
[52] Jin L. *et al.*, *Phys. Rev. B*, **102** (2020) 125118.
[53] Hastings K. W., *Biometrika*, **57** (1970) 97.
[54] Griffith S. J., *J. Chem. Phys.*, **41** (1964) 576.
[55] Matthes L. *et al.*, *J. Phys.: Condens. Matter*, **5** (2013) 395305.
[56] Thouless D. J. *et al.*, *Phys. Rev. Lett.*, **49** (1982) 405.
[57] Xiao D. *et al.*, *Rev. Mod. Phys.*, **82** (2020) 1959.
[58] Soluyanov A. A. and Vanderbilt D., *Phys. Rev. B*, **83** (2011) 235401.
[59] Taherinejad M. *et al.*, *Phys. Rev.*, **89** (2014) 115102.
[60] Souza I. *et al.*, *Phys. Rev. B*, **65** (2012) 035109.
[61] Cong R. *et al.*, *J. Phys.: Condens. Matter*, **32** (2020) 405802.
[62] Sheng X. L. and Nikolic B. K., *Phys. Rev. B*, **95** (2017) 201402.
[63] Sarikurt S. *et al.*, *Phys. Chem. Chem. Phys.*, **20** (2018) 997.
[64] Jackeli G. and Khaliullin G., *Phys. Rev. Lett.*, **102** (2009) 017205.